

Research Article

Fatigue Fracture Properties and Morphology of Polyoxymethylene (POM) Plates Produced under Moderate Processing Conditions

M. Berer ¹, M. Halb,¹ M. Feuchter,² G. Pacher,¹ and G. Pinter²

¹Polymer Competence Center Leoben GmbH, Roseggerstrasse 12, 8700 Leoben, Austria

²Material Science and Testing of Polymers, Montanuniversitaet Leoben, Otto Gloeckel-Strasse 2, 8700 Leoben, Austria

Correspondence should be addressed to M. Berer; michael.berer@pccl.at

Received 12 April 2018; Revised 27 July 2018; Accepted 5 August 2018; Published 4 November 2018

Academic Editor: Vito Speranza

Copyright © 2018 M. Berer et al. This is an open access article distributed under the Creative Commons Attribution License, which permits unrestricted use, distribution, and reproduction in any medium, provided the original work is properly cited.

The present study was inspired by different industry projects in which a strong dependence of the fatigue fracture performance of POM on the processing conditions was observed. To examine the relationships under more reproducible conditions, plates of two different POM homopolymer resins (one significantly nucleated) were produced by compression molding and by injection molding under moderate conditions. For the injection molding, three different mold temperatures were used. At specific locations, the plates were analyzed concerning their hierarchical structure on the micro- and nanolevel and concerning their fatigue fracture performance. For the fatigue fracture performance, the dependence on the processing conditions was rather small for the nucleated resin but much more significant for the other resins. This dependence could not be related to morphological effects only, and thus, a combined effect of morphology and residual stresses was assumed.

1. Introduction

POM is a semicrystalline, thermoplastic polymer with high degrees of crystallinity. It is frequently used for components which are exposed to cyclic loading [1–7], and hence, its fatigue properties are of technical interest. Generally, this material shows only small crack tip plasticity in fatigue crack growth tests, and thus, it can be investigated quite well using linear elastic fracture mechanics [8–16].

It is state of the art that changes in the morphology of polymers, which are introduced by varying processing parameters, additives, physical ageing, postcrystallization, or annealing, have an influence on the resulting crack growth behavior. In the literature, this is mainly attributed to changes in the tie molecule and entanglement densities [13, 17–21]. However, the determination of the latter is very complex and time-consuming [13, 20], and thus, easier accessible parameters are usually used to correlate changes in the crack growth behavior with the corresponding changes in the morphology. This strategy was also used in the present study, and the morphology was interpreted in terms of (mass and volumetric) degree of crystallinity and amorphous

fraction, long period, lamellar thickness and thickness of the amorphous layer, contribution of the different X-ray diffraction peaks, spherulite size and size distribution, and the cross-sectional (“skin–core”) layer structure.

Generally, the number of publications focusing on the interactions between processing conditions, resulting material morphology and mechanical properties of polymers, is not so small. However, this number becomes significantly smaller when only those are considered, which examine the full chain (starting with processing and ending with the mechanical properties) and not only parts of it. From a material’s point of view, so far, most of the work was done for polypropylene [18, 22–35], which seems to be the best studied polymer in this field. Nevertheless, aside from studies done on other polymers [17, 36, 37], there are surprisingly many publications available for POM [13, 19, 23, 38–40] as well. These POM studies have quite different motivations and approaches. Runt and Gallagher [13] used a combination of quenching, annealing, and isothermal crystallization to obtain specimens with different morphologies, which were analyzed and compared for their fatigue fracture properties (crack growth kinetics). In [19, 38], the decrease of the

fracture toughness (K_{IC}) in dependence on the crystallization temperature used in compression molding was modelled (via the loss in entanglement density) and experimentally verified. These three studies are of scientific interest mainly since the annealing and crystallization temperatures examined were rather high (100–160°C) and thus usually not relevant for conventional processing conditions. Zhao and Ye [40] studied the effect of drawing (different draw ratios) on morphology and mechanical properties of POM. Most relevant for our study are the publications of Wright et al. and Viana [23, 39] in which POM was injection-molded using conventional processing conditions. However, in both studies, the morphological analysis is incomprehensive and the mechanical characterization focuses more on monotonic properties (tensile and fracture toughness tests) than on the fatigue fracture performance.

The present study was inspired by different industry projects in which a strong dependence of the fatigue fracture performance of POM on the processing conditions was observed. To examine the relationships under more reproducible conditions, moderate processing conditions were selected. For this, two POM homopolymer resins (one significantly nucleated) were processed by compression molding and by injection molding under moderate conditions. The molded plates were analyzed concerning their fatigue crack growth behavior (cyclic fatigue fracture tests) and concerning their morphology. The material morphology was characterized using differential scanning calorimetry (DSC), polarized light microscopy (PLM), small-angle X-ray scattering (SAXS), and wide-angle X-ray diffraction (WAXD).

2. Materials and Methods

The basic work of this study was conducted within a diploma thesis at the Polymer Competence Center Leoben, which is recommended as reference for more specific information concerning the experimental details [41].

2.1. Materials and Processing. Two different POM homopolymer resins were examined in this study: Delrin 111PF from DuPont (DuPont, Wilmington, Delaware, USA) and Tenac 3010 from Asahi Kasei (Asahi Kasei, Tokyo, Japan). The Delrin resin is a special grade, which is based on Delrin 100 but with modifications in the additive contents. The most relevant modification for this study is that it contains a heterogeneous nucleation agent to improve the fatigue crack growth behavior. The materials will be called “Delrin” and “Tenac” in the following discussions. For both resins, the molecular weight and the polydispersity index are given in Table 1. For Tenac, this data was already published previously [15]. The corresponding data for the Delrin resin used in this study was also determined at that time.

Both materials were processed by the same processing techniques, i.e., compression molding and injection molding with three different mold temperatures. For compression molding, the molding press “Collin PCS II” (Dr. Collin GmbH, Ebersberg, Germany) was used. The corresponding compression molding parameters are listed in Table 2. The injection molding machine used was an “Arburg Allrounder

TABLE 1: Molecular characteristics of the POM resins used in this study.

Material	Weight (average molecular weight) M_w (g/mol)	Polydispersity index
Delrin	149,000	2.6
Tenac	137,000	2.6

TABLE 2: Processing parameters used for compression molding (plate dimension: 150 × 150 × 4 mm).

	Heating	Compression	Cooling
<i>Delrin</i>			
Pressure (bar)	1	100	100
Temperature (°C)	210	210	30
Time span (min)	16	15	18
<i>Tenac</i>			
Pressure (bar)	1	100	100
Temperature (°C)	210	210	30
Time span (min)	18	15	18

470A 1000-400 Alldrive” (Arburg GmbH & Co. KG, Loßburg, Germany). The settings for the most important injection molding parameters are given in Table 3. The processing parameters for both techniques were based on the corresponding data sheets provided by the material producers. Nevertheless, they had to be adapted empirically to gain acceptable component quality. In order to guarantee comparability between the two resins, the processing conditions were kept as constant as possible. However, slight adaptations of some processing parameters could not be avoided in order to achieve similar component quality. In both techniques, plates with a side length of 150 × 150 mm were produced. Due to the different molds available, the thickness was not uniform; the compression-molded plates had a thickness of 4 mm, while the injection-molded ones were 5 mm thick. In all cases, the material was dried before processing. This was an important detail because without drying, an insufficient plate quality was obtained in compression molding as well as injection molding. For the compression molding, the dried granules were used directly (no previous melting). The amount required was uniformly distributed in a steel frame and subsequently heated and compressed in the molding press using the processing parameters in Table 2. In case of injection molding, filling studies for all mold temperatures and resins were conducted directly before the molding of the plates. They confirmed a symmetrical filling of the mold in all cases. This was especially important for the definition of the characterization spots.

2.2. Analysis Techniques

2.2.1. SAXS and WAXD. In order to facilitate the comparison between morphology and fracture mechanical properties, the SAXS and WAXD analysis was carried out directly on the compact tension (CT) specimens used for the subsequent fracture mechanical tests. The specimens were made from the plates as described below. In analogy to [15], the

TABLE 3: Processing parameters used for injection molding (plate dimension: $150 \times 150 \times 5$ mm).

	Delrin	Tenac
Screw diameter (mm)		40
Metering volume (cm^3)		160
Back pressure (bar)		40
Melt temperature ($^{\circ}\text{C}$)	215	210
Injection flow rate (cm^3/s)		10
Max. injection pressure (bar)	700	630/700 (90 $^{\circ}\text{C}$ mold temperature only)
Mold temperature ($^{\circ}\text{C}$)		60/90/110
Switch-over volume (cm^3)		27
Holding pressure (bar)		600
Holding pressure time (s)		12
Remaining cushion (cm^3)	12	11
Residual cooling time (s)		50
Total cycle time (s)	82.8	80.8

measurement position for the X-ray measurements was about 2.5 mm ahead of the premilled notch of the CT specimens. Based on our experience with fatigue fracture testing of POM, it was expected that this area is passed by the crack during fatigue crack growth. The measurements were conducted for both resins, all processing conditions, and all position variations except for those made from the injection-molded plates and rotated by 90 $^{\circ}$ (crack orientation perpendicular to the flow direction). They were expected to show the same morphology as the specimens, which were not rotated (crack orientation in flow direction). For the details regarding the CT specimen alignment on the plates, please refer to the corresponding section below. For each condition examined, 5 CT specimens were analyzed using SAXS and WAXD before the fatigue fracture tests were conducted.

All SAXS and WAXD experiments were conducted on a Bruker NANOSTAR (Bruker Corporation, Massachusetts, USA). The X-ray source I μ S (Incoatec GmbH, Geesthacht, Germany) provided monochromatic radiation with a wavelength of 1.54 \AA . The X-ray beam was focused by a circular aperture to a diameter of 300 μm . SAXS and WAXD tests were performed simultaneously using the setup shown in Figure 1. The exact distances between samples and detectors were determined using a silver behenate standard for the SAXS detector and a silicon standard for the WAXD detector. For all measurements, an irradiation time of one hour was used. A software tool called “Fit2d” (European Synchrotron Radiation Facility, Grenoble, France) was used for the integration of the SAXS and WAXD patterns [42]. The integrated patterns will be termed as “profiles” in the subsequent discussion.

For SAXS, an automatic detector of the type “VÅNTEC-2000 2D MicroGap” (Bruker Corporation, Massachusetts, USA) was used. The radial integration of the recorded patterns was done up to a scattering angle of 1.5 $^{\circ}$. For the morphological interpretation of the SAXS profiles, two different methods were used: the so-called “1D correlation” [43, 44] and a fitting procedure, which uses a 3-component model developed especially for POM [21, 45, 46]. The background

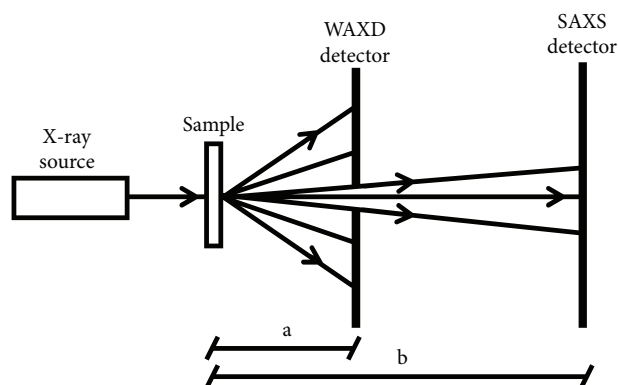


FIGURE 1: Setup for simultaneous SAXS and WAXD measurements (a was 49.9 mm for all measurements, b was 1142.5 mm for the plate scanning and 1097 mm for the CT specimen measurements).

for this proceeding was that for POM it is nowadays accepted that there are three different phases (two different types of crystalline lamellae and the amorphous phase) present in a conventionally crystallized material [1, 21, 45–47]. Since 1D correlation is based on a two-phase model, a part of the morphology information is lost, when using this analysis technique. This loss of information can be prevented when using the 3-component model developed by Hama and Tashiro [21, 46]. However, to the best knowledge of the authors, this method has not been applied on such high molecular weight resins as used in this study so far. Hence, its applicability for our purposes was unclear at the beginning. For both methods (1D correlation and 3-component model), a self-written MATLAB (MathWorks Inc., Natick, Massachusetts, USA) script was used for the analysis and parameter calculation.

In accordance with the literature [43, 44], the 1D correlation script allowed the extrapolation of the scattering profiles on both ends to overcome the experimental limitations and calculated the correlation function afterwards. For the extrapolation at high q , a modified Porod law assuming a

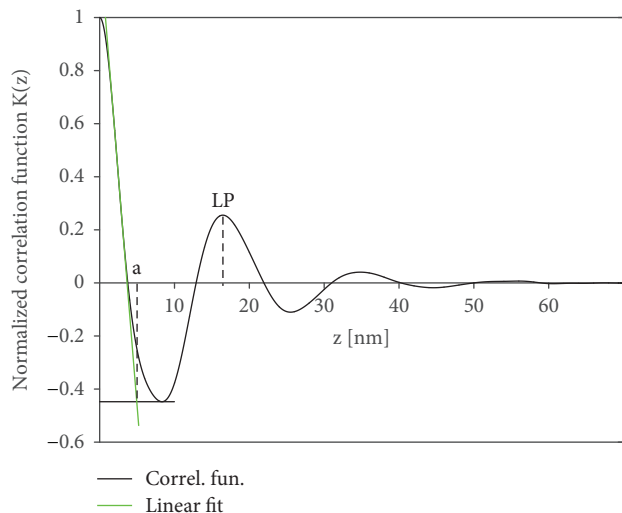


FIGURE 2: Example for the correlation functions obtained (Delrin, injection molded, 110°C mold temperature, CT specimen, “Delrin_IM_110°C-MT”) and scheme of the analysis used.

sigmoidal electron density transition [48, 49] was fit to the tail of the intensity profile. The background scatter, which was obtained as a fit result, was subtracted from the whole profile. Since the measured intensities were not obtained as absolute values, the normalized correlation function was created. The analysis of the correlation functions was done as illustrated in Figure 2. Although no plateau was observed at the first minimum, the latter was used for the determination of the layer thicknesses and linear crystallinity. It is expected that this simplification is a good engineering approach in our case because the layer thicknesses obtained were mainly used for the comparison of comparatively similar material conditions at one temperature (room temperature). Nevertheless, it has to be kept in mind that the values are only an estimation of the “real” layer thicknesses. The layer thicknesses and linear crystallinities were also calculated based on the first zero of the correlation function. However, according to our experience from an internal study (in which a layer-by-layer SAXS and WAXD analysis was conducted on some of the plates used in this study), these values are not very reliable for our materials especially for the Delrin resin. Hence, the plateau values were preferred. The script for the implementation of the 3-component model fitted this model to the measured SAXS data using a nonlinear least squares optimization. For the conversion between layer thicknesses, long period, and “linear crystallinity” (volumetric degree of crystallinity within the crystalline stack [50]), (1) (1D correlation) and (2) (3-component model) were used, respectively.

$$X_{C,1D,>50\%} = 1 - \frac{a}{LP}, \quad (1)$$

where a is the amorphous layer thickness and LP is the long period (both obtained from 1D correlation). $X_{C,1D}$ is the volumetric degree of crystallinity in the crystalline stack based on the 1D correlation results. The formula

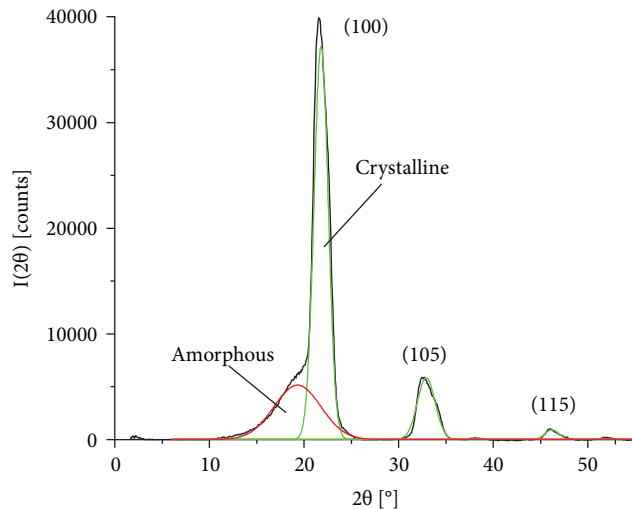


FIGURE 3: Schematic illustration of the analysis of the WAXD profiles including the peak used for the amorphous halo.

above is valid only for materials with a crystallinity of more than 50% [44], which was the case for the POM materials examined in this study.

$$X_{C,3comp} = \frac{d_1 + d_2}{LP}, \quad (2)$$

where d_1 and d_2 are the lamellar thicknesses of “folded chain lamellae” and “extended chain lamellae”, respectively [21, 45, 46]. All parameters are fitting coefficients of the 3-component model. $X_{C,3comp}$ is the volumetric degree of crystallinity in the crystalline stack based on the 3-component model.

For the WAXD measurements, an analogue detector was used. It was placed directly in the test chamber with a distance of 49.9 mm to the sample (Figure 1). The detector had a central hole so that the scattered SAXS beam could pass. After every measurement, the detector was removed from the chamber and digitized, and finally, the detected pattern was deleted before starting the next measurement. The WAXD profiles generated from the patterns were analyzed concerning the (mass) degree of crystallinity (3) and regarding the contribution of the different diffraction peaks to the total area. For the determination of the amorphous fraction, the amorphous halo was defined in a similar way as shown in [40] (a more regular peak shape was used in our case). The analysis procedure is illustrated in Figure 3.

$$X_{C,WAXD} = \frac{a_c}{a_c + a_a}, \quad (3)$$

where a_c and a_a are the total area under the crystalline peaks and the area of the amorphous halo, respectively. $X_{C,WAXD}$ is the (mass) degree of crystallinity obtained from WAXD.

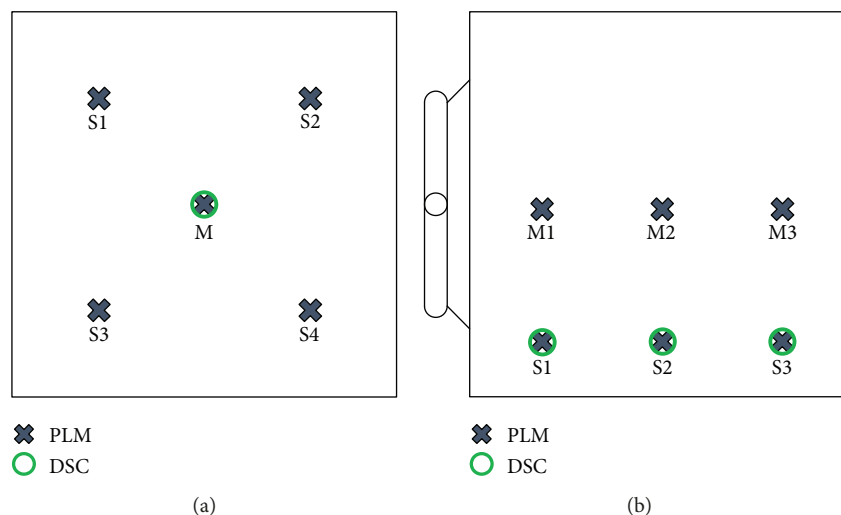


FIGURE 4: Sample positions used for the PLM studies and the DSC measurements. Compression-molded plate (a) and injection-molded plate (b).

2.2.2. *PLM*. PLM (polarized light microscopy) was used to qualitatively examine the cross section microstructure of the differently processed POM plates. This comprised the spherulite size and distribution as well as the layer structure introduced through injection molding.

The PLM analysis was conducted on the plates only. For each processing condition, one selected plate was analyzed. The samples used for the analysis were thin films, which were prepared in a way that the entire thickness of the plate could be examined. They were taken from multiple positions of the molded plates, which are marked in Figure 4 (S stands for side and M for middle). For the analysis, it was assumed that the compression-molded plates were homogenous and that the injection-molded plates were symmetric in the flow direction. The latter assumption was supported by the previously conducted filling studies. For the preparation of the films, the plates were first cut into stripes with a buzz saw to get close to the measuring points; the injection-molded plates were cut in filling direction, while the compression-molded plates had no preferred direction. Then, several layers of the cut face were removed with a microtome to exclude any influence of the saw cutting on the microstructure and to make the surface smooth and clean. Finally, the sample films, which had a thickness of 10 μm , were cut off with the microtome. They were placed on a microscope slide and fixed with baby oil and a thin glass plate.

The PLM images were recorded on an “Olympus SZX12 stereo microscope” (Olympus Corporation, Tokyo, Japan). For this, the samples were placed between two crossed polarizers (twisted by 90°) and the images were made using the transmitted light mode.

2.2.3. *DSC*. The samples used for the differential scanning calorimetry (DSC) were taken from the same plates as those for the PLM. However, as shown in Figure 4, only selected points were analyzed using DSC (compression-molded plates: position “M”; injection-molded plates: positions “S1,” “S2,” and “S3”). Based on our experiences from

TABLE 4: Temperature profile used for the DSC measurements.

1 st heating run	Hold	Cooling run	Hold	2 nd heating run
25°C → 230°C	230°C	230°C → 25°C	25°C	25°C → 230°C
10 K/min	3 min	10 K/min	3 min	10 K/min

previous studies, the authors consider DSC as a rather rough method for the determination of the crystallinity of POM. Hence, the analysis was limited to the compression-molded plates and to the injection-molded plates processed with 90°C mold temperature. After preparing the samples for PLM, small pieces with 5–7 mg of weight were cut off the remaining parts of the plates with a cutter. Because each sample was intended to represent the entire thickness of the plate, thin rods with 4 mm (for the compression-molded plates) and 5 mm (for the injection-molded plates) in length, respectively, were obtained. The samples were put into 40 μl aluminum crucibles and sealed with caps with two holes for pressure compensation. For each measurement position, in total thirteen DSC measurements were conducted.

The DSC measurements were done on a “DSC 1 STAR^e System” (Mettler-Toledo International Inc., Columbus, Ohio, USA). Before the measurements, the calibration of the machine was checked using a standard indium sample. All samples were tested using the same temperature profile given in Table 4. The degree of crystallinity ($X_{\text{C,DSC}}$) of the samples was calculated using (4).

$$X_{\text{C,DSC}} = \frac{\Delta H}{\Delta H_0} * 100, \quad (4)$$

where ΔH_0 is the specific melt enthalpy of 100% crystalline POM, which is 250 J/g according to [38]. ΔH is the specific melt enthalpy measured in the DSC tests (1st heating run). $X_{\text{C,DSC}}$ is the mass degree of crystallinity obtained by DSC.

2.2.4. *Fatigue Fracture Tests*. Fatigue fracture tests were selected for the fracture mechanical characterization

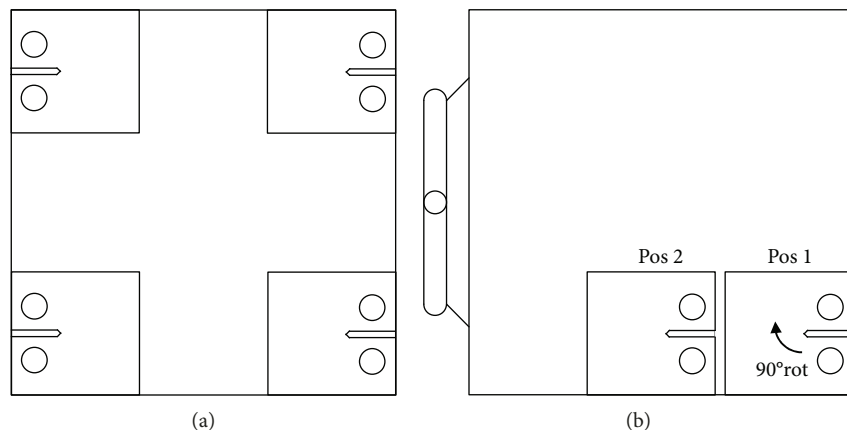


FIGURE 5: Alignment of the CT specimens on the compression-molded plates (a) and on the injection-molded plates (b).

TABLE 5: Load levels used for the fatigue fracture tests (F_{\max} , F_{\min} are the maximum and minimum load of the sinusoidal signal, respectively).

	Data point	1	2	3	4
Compression-molded CT specimens	F_{\max} (N)	400	440	460	520
	F_{\min} (N)	40	44	46	52
Injection-molded CT specimens	F_{\max} (N)	500	550	575	600
	F_{\min} (N)	50	55	57.5	60

because they are known to be very useful for material ranking [15, 16]. Moreover, they were found to be very sensitive on morphological changes [13, 15, 17, 51]. In general, the method used in this study is based on the recently approved standard ISO 18489 [52]. However, CT specimens instead of the recommended cracked round bar (CRB) specimens were used in our case because they can be produced of thinner plates. The applicability of this specimen type for POM tested under similar testing conditions was shown in previous studies [14, 15]. As it is suggested in the attachment of ISO 18489 [52], the stress intensity factor was used to express the local load level inside the specimens (ahead of the crack tip). The aim of the fatigue fracture tests was to determine the number of cycles to final fracture in dependence on the initial stress intensity factor amplitude (ΔK_{init}). The corresponding diagrams will be termed “fatigue fracture curves” in the following discussions.

The CT specimens were prepared from the molded plates using a mill cutter. The positions where they were taken from are given in Figure 5. For the injection-molded plates with 60°C and 110°C mold temperature, the specimens were taken from position 1 only. For the injection-molded plates with 90°C mold temperature, the specimens were taken from positions 1 and 2 in order to examine areas near and far from the sprue. Additionally, specimens from position 1 but rotated clockwise by 90° were made for this mold temperature in order to investigate the dependence of the fatigue fracture performance on the melt flow direction (in Results and Discussion, these samples will have the suffix “Pos1-90°rot” in their name). The CT specimens were made with a specimen width W of 40 mm. Because of the different processing techniques used, they had two different thicknesses: 4 mm (compression-molded plates) and 5 mm (injection-

molded plates). Directly before the measurements, the pre-milled notch was sharpened with a razor blade (geometry (approximate values): thickness 0.1 mm, tip radius 1–2 μm , opening angle 15°) to generate a defined and uniform initial crack geometry.

The tests were carried out on a servohydraulic testing machine of the type “MTS 858 horizontal” (MTS System Corporation, Minneapolis, Minnesota, USA). A load ratio R (minimum load/maximum load) of 0.1 and a frequency of 10 Hz (sinusoidal signal) were used for all measurements. All tests were done in load-controlled mode. For both resins, all processing conditions and all position variations examined, one complete fatigue fracture curve was generated. Each of them consisted of four measurement points tested at four different load levels. The corresponding load values are shown in Table 5. Because of the different plate thicknesses and fatigue fracture resistances, these load values were different for compression- and injection-molded plates. Following ISO 18489 [52] and owed to the long test duration of fatigue tests, for each load level, only one single specimen was tested. Based on our experience with previous tests made on POM and confirmed by the present experiments, the scatter between the tests is sufficiently small to allow this proceeding.

3. Results and Discussion

From a currently running study, we know that POM can show significant post processing changes when stored at room temperature. This is important because several months were required to finish the characterization program of the plates. However, since in this work the materials were

TABLE 6: SAXS measurements of the CT specimens analyzed using 1D correlation (LP is the long period, a is the thickness of the amorphous layer, l is the lamellar thickness of the crystalline lamella).

CT specimens	LP ¹ (nm)	a ¹ (nm)	l ¹ (nm)	Crystallinity ² (vol%)	Amorphous fraction ² (vol%)
Delrin_CM	17.2 ± 0.2	4.8 ± 0.1	12.4 ± 0.2	72.0	28.0
Delrin_IM_60°C-MT	14.6 ± 0.1	4.6 ± 0.1	10.0 ± 0.1	68.5	31.5
Delrin_IM_90°C-MT_Pos1	15.5 ± 0.1	4.9	10.6	68.7	31.3
Delrin_IM_90°C-MT_Pos2	15.4 ± 0.1	4.7 ± 0.1	10.7 ± 0.1	69.4	30.6
Delrin_IM_110°C-MT	16.4 ± 0.1	5.0	11.5	69.8	30.2
Tenac_CM	16.3 ± 0.2	4.8 ± 0.1	11.5 ± 0.1	70.7	29.3
Tenac_IM_60°C-MT	14.2	4.7 ± 0.1	9.5 ± 0.1	66.7	33.3
Tenac_IM_90°C-MT_Pos1	15.1	4.9 ± 0.1	10.2 ± 0.1	67.6	32.4
Tenac_IM_90°C-MT_Pos2	15.2	4.9	10.3	67.5	32.5
Tenac_IM_110°C-MT	15.9	5.1 ± 0.1	10.9 ± 0.1	68.2	31.8

¹Average value ± standard deviation (if the latter is not given it is smaller than 0.05). ²Average value.

TABLE 7: WAXD measurements of the CT specimens analyzed for the contribution of the different diffraction peaks to the total crystallinity.

CT specimens	Crystallinity ¹ (%)	(100) ² (%)	(105) ² (%)	(115) ² (%)	(205) ² (%)	Amorphous fraction ² (%)
Delrin_CM	75.8 ± 0.8	60.1	12.2	2.9	0.6	24.2
Delrin_IM_60°C-MT	72.6 ± 1.0	60.4	10.6	1.4	0.1	27.4
Delrin_IM_90°C-MT_Pos1	75.1 ± 0.9	62.0	11.2	1.7	0.2	24.9
Delrin_IM_90°C-MT_Pos2	75.9 ± 0.7	64.1	10.2	1.5	0.2	24.1
Delrin_IM_110°C-MT	74.3 ± 0.3	61.2	11.4	1.6	0.2	25.7
Tenac_CM	74.8 ± 0.5	58.6	12.6	3.0	0.7	25.2
Tenac_IM_60°C-MT	70.7 ± 0.7	57.0	11.8	1.7	0.2	29.3
Tenac_IM_90°C-MT_Pos1	70.5 ± 0.8	56.4	12.1	1.7	0.3	29.5
Tenac_IM_90°C-MT_Pos2	71.6 ± 0.6	58.0	11.7	1.7	0.2	28.4
Tenac_IM_110°C-MT	71.3 ± 0.4	56.9	12.3	1.8	0.3	28.7

¹Average value ± standard deviation. ²Average value.

processed under comparatively moderate conditions, the aging effect is expected to be of minor importance.

In order to facilitate the readability of this section, a uniform nomenclature is used for the different plates/samples/specimens examined. The following abbreviations are used in this context:

- (i) “CM” for compression molding and “IM” for injection molding
- (ii) “MT” is the mold temperature used in injection molding
- (iii) “M,” “M1,” “M2,” “M3,” “S1,” “S2,” “S3,” and “S4” are the position indicators for the PLM and DSC samples (in accordance with Figure 4)
- (iv) “Pos1,” “Pos2,” and “Pos1-90°rot” give details about the CT specimen alignment on the injection-molded plates processed with 90°C mold temperature (in accordance with Figure 5)

3.1. Material Morphology

3.1.1. SAXS and WAXD. The results of the SAXS and WAXD measurements made on the CT specimens are summarized

in Tables 6 and 7. The values given in these tables are averages of five measurements. In Table 6, the results of the SAXS measurements analyzed using 1D correlation are given. For both materials, the CT specimens made of the compression-molded plates have the biggest long periods and lamellar thicknesses. The amorphous layer thicknesses, on the other hand, are similar to those of the injection-molded samples. For the CT specimens made of the injection-molded plates, long period, lamellar thickness, and amorphous layer thickness increase with increasing mold temperature. However, even for the highest mold temperature used (110°C), the long period and lamellar thickness do not reach the levels of the compression-molded specimens. In comparison to Tenac, the Delrin specimens reveal slightly higher long periods and lamellar thicknesses. For the amorphous layer thicknesses, both materials show very similar values. The two different positions, which were examined for the injection-molded plates with 90°C mold temperature (“Pos1” and “Pos2” in Table 6), show no significant differences in long period, lamellar thickness, and amorphous layer thickness.

In addition to the long period and layer thicknesses, the (volumetric) degree of crystallinity was calculated using (1). The highest values for this parameter are observed for the

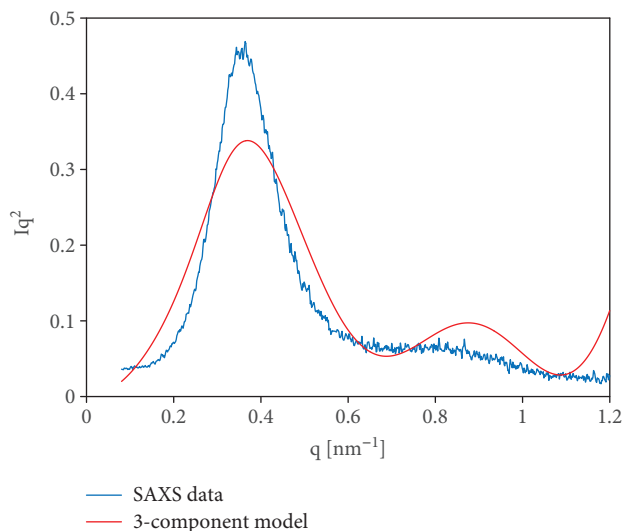


FIGURE 6: Representative result of the 3-component model fit (SAXS data belongs to the Delrin_IM_110°C-MT sample).

compression-molded CT specimens. For the specimens made of the injection-molded plates, only a small increase with increasing mold temperature is observed. For the two materials examined, Delrin shows the slightly higher degree of crystallinity in all processing conditions used. However, it is evident from Table 6 that the changes in the (volumetric) degree of crystallinity are less pronounced than those in long period and lamellar thickness.

As described above in Materials and Methods, a second analysis method for the SAXS data was used in this study: a fitting procedure, which uses a 3-component model developed especially for POM [21, 45, 46]. The background for this proceeding was, as mentioned before, that for POM it is nowadays accepted that there are three different phases (two different types of crystalline lamellae and the amorphous phase) present in a conventionally crystallized material [1, 21, 45–47]. Since 1D correlation is based on a two-phase model, a part of the morphology information is lost, when using this analysis technique. This loss of information can be prevented when using the 3-component model developed by Hama and Tashiro [21, 46]. However, for our SAXS data, no reasonable results were obtained with this analysis method. Although a lot of effort was made (many different starting points for the fit were tried, even ridiculous ones), the fitting quality achieved was not acceptable. During the analysis procedure, the 3-component model generally caused some doubts about its reliability. Figure 6 is a representative for all fitting results; it was generally observed that the first peak in the Lorentz-corrected SAXS profile was underestimated by the fit, whereas the second one was overestimated, and the peak maxima of the data and the fit did not coincide. Additionally, a further, rather significant peak was observed in the fit results, which started at a q -value of approximately 1.1 nm^{-1} . This additional peak was always obtained, and hence, the diagrams were truncated at 1.2 nm^{-1} as it was done by Hama and Tashiro in their papers [21, 46]. From personal communications, we know that an additional peak

at higher q levels was also observed by other working groups. It is speculated if this peak is not an erroneous artefact of the model. The described issues were observed similarly for Delrin and Tenac. Based on the observations made and although Hama and Tashiro mentioned Delrin and Tenac in their work [21], the applicability of the 3-component model for these two materials is questionable at least for the high molecular weight resins used in our study.

For the analysis of the WAXD data given in Table 7, two main aspects are taken into account: the (mass degree of) crystallinity and the quality of the crystal packing. The latter is deduced from the contribution of the crystal peaks located at higher diffraction angles to the total area of the WAXD profile. The compression-molded samples show both, slightly higher crystallinity and higher quality of the crystal packing (higher contribution of (105), (115), and (205) diffraction peaks) than the injection-molded ones. For the injection-molded CT specimens, the quality of the crystal packing does not change a lot with the mold temperature. In addition, the increase in crystallinity is rather small when taking into account the standard deviation. However, the increase is more pronounced for Delrin than for Tenac. For both processing techniques used (compression molding and injection molding), Delrin shows a higher level of crystallinity. The comparison of the CT specimens obtained from plate positions 1 and 2 (“Pos1” and “Pos2” in Table 7) shows that at position 2 the total crystallinity is similar or slightly higher, but the quality of the crystal packing is lower (higher fraction of (100), smaller or similar fraction of (105), (115), and (205)). For the SAXS results, such a position dependence was not observed.

For the interpretation of the SAXS and WAXD results, it has to be kept in mind that the whole cross section was examined. Hence, the quantitative results for crystallinities, long periods, layer thicknesses, and diffraction peak contributions (to the overall crystallinity) represent average values along the thickness. To obtain this information on a local scale, a layer-by-layer SAXS/WAXD analysis was carried out as a follow-up to the present study. The analysis was made for selected conditions of the ones discussed in this study. However, the additional information obtained from this layer-by-layer analysis was rather limited. It was shown that on this local scale the influence of sample preparation and analysis parameters becomes dominant. Hence, the corresponding results are not implemented in the present study.

3.1.2. PLM. In the following, the cross section microstructure of the compression- and injection-molded plates will be discussed for both materials. In all cases, the PLM images selected are representative for the condition examined. In Figure 7, the images of the compression-molded plates are given. Due to the added heterogeneous nucleation agent, the compression-molded Delrin sample (Figures 7(a) and 7(b)) has a very fine structure over the entire thickness. A rough estimation of the spherulite diameters observed in Figure 7(b) gave an approximate diameter range of 25–50 μm . A skin region at the surface cannot be observed for this sample, which leads to the conclusion that Delrin does not form a skin layer when processed by compression

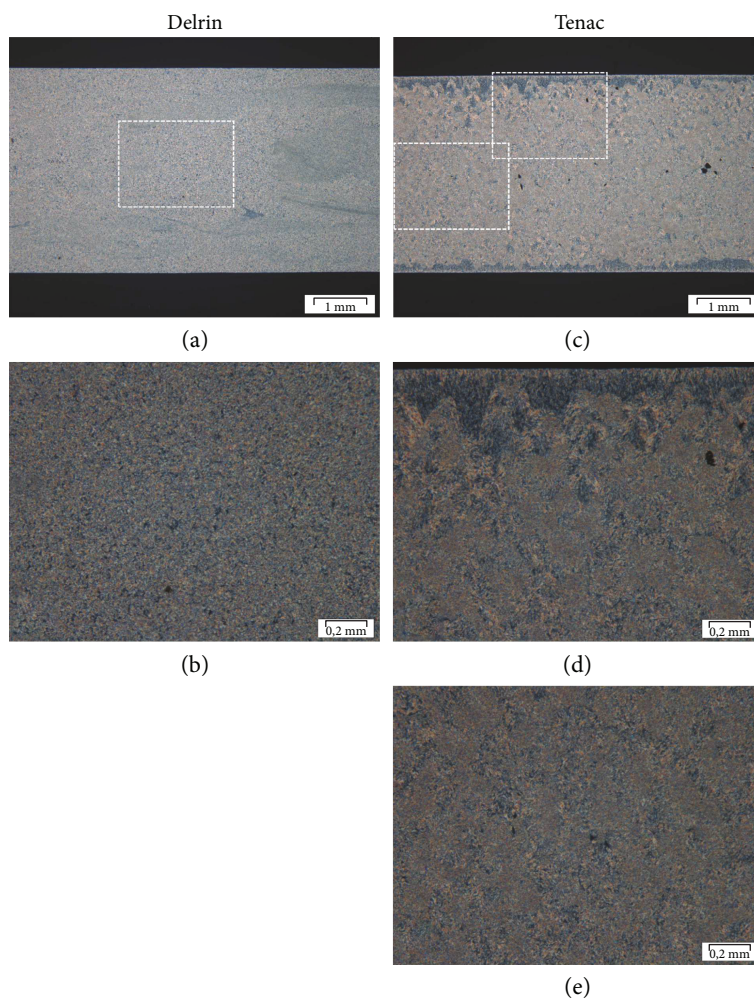


FIGURE 7: PLM images of the cross section of compression-molded plates. Overview and details for Delrin (a, b) and Tenac (c–e).

molding with the processing conditions used. There are “fuzzy” areas distributed irregularly over the plate, which were observed at all five sample positions shown in Figure 4. They seem to contain even finer spherulites than the rest of the material. Their origin has not been identified yet, but they are assumed to represent the transition zone between adjacent granulate grains of the resin.

Compared to Delrin, the compression-molded Tenac plate (Figures 7(c)–7(e)) has a much coarser structure and a distinct skin layer. A skin layer for the compression-molded plate was rather unexpected since the cooling conditions were very moderate. However, this skin layer was observed at all five sample positions investigated. It is shown in Figure 7(d) with a higher magnification. The area directly below the plate surface shows less pronounced crystal structures (no spherulites) than the rest of the sample. Below, irregular-shaped spherulites with longitudinal orientation towards the center of the plate can be observed (size approximately 100–250 μm). Below a depth of about 0.15 mm, the microstructure is dominated by spherulites with regular shape (rough diameter range is 100–250 μm). Towards the center of the plate, the spherulite sizes do

not change further but the overall spherulitic structure becomes more and more compact.

As it is illustrated in Figures 8–11, the microstructure of the injection-molded plates was found to be more complex than that of the compression-molded ones. In Figures 8 and 9, the corresponding PLM images of Delrin and Tenac are shown for the different mold temperatures used in the injection molding process. They are aligned along the filling direction from near the sprue to far from the sprue (in accordance with the positions “S1,” “S2,” and “S3” in Figure 4). The “S” positions were selected because the CT specimens used for the fracture mechanical tests were also made of this area. The PLM images at the “M” positions were very similar to the corresponding “S” position images.

In the following, the layer structure observed will be discussed with respect to previous findings in the literature. Liparoti et al. determined a general structure for injection-molded polypropylene plates, which consists of the following three layers starting from the outside [26]:

- (i) Skin layer with two subphases

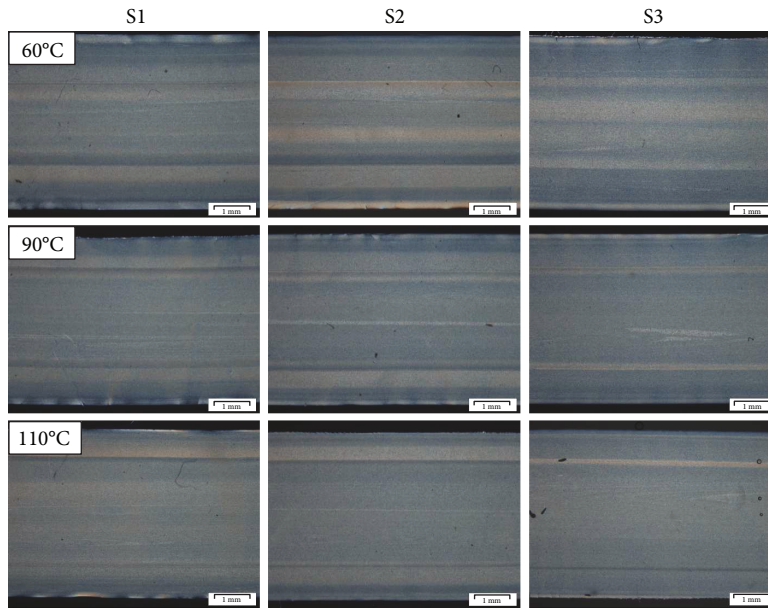


FIGURE 8: PLM images of the cross section of injection-molded Delrin plates in dependence on the distance from the sprue and on the mold temperature used.

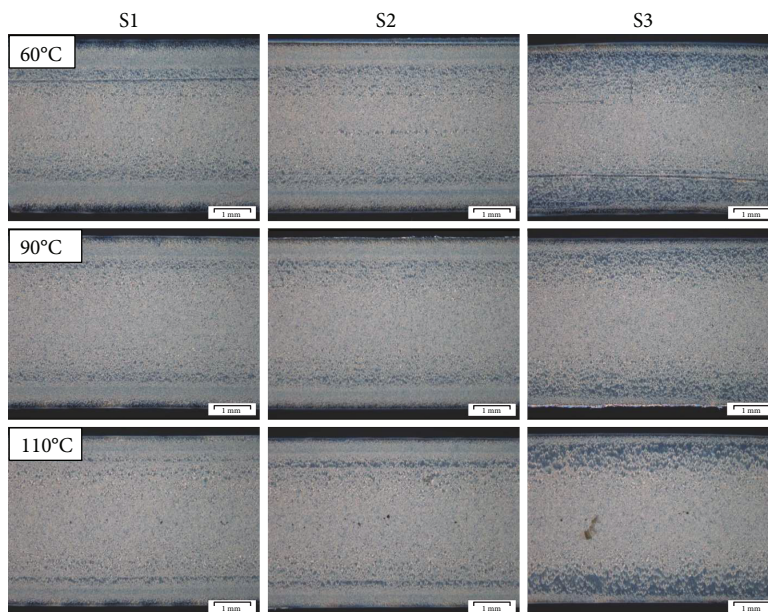


FIGURE 9: PLM images of the cross section of injection-molded Tenac plates in dependence on the distance from the sprue and on the mold temperature used.

- (ii) Shear layer with structures aligned along the flow direction
- (iii) Spherulitic layer in the central zone of the plate

The study of Liparoti et al. is the most elaborated one concerning the layer structure of unfilled and injection-molded semicrystalline thermoplastics. Although it was conducted for an alternative material (polypropylene), it will be used as reference in this work.

For Delrin, a quite distinct layer structure with numerous layers and very fine spherulites can be observed in Figure 8. This layer structure does not correlate well with what was observed by Liparoti et al. for polypropylene. As a rough trend, the number of layers decreases from low to high mold temperature and from near the sprue (“S1”) to far from the sprue (“S3”). It seems that the lower the temperature difference between the mold and the melt, the less layers appear. It is interpreted that most of the additional layers represent

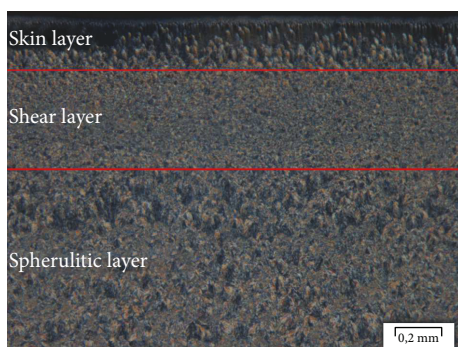


FIGURE 10: Layer structure of the injection-molded Tenac plates (PLM image of “Tenac_IM_90°C-MT_S1”).

additional shear zones because of the quite fast solidification of the nucleated Delrin resin in the mold. Far from the sprue, the number of layers decreases because less material has to pass this area and thus less material shearing occurs. A classical skin layer with less pronounced crystal structures is only observed for the “harshes” conditions used (“Delrin_IM_60°C-MT-S1”: 60°C mold temperature and close to the sprue). Even in this case, the thickness of this skin layer is very small (in the order of 50 μm). Besides the thinner layers, three main layers can be distinguished in Figure 8 (especially for the samples with high mold temperature and far from the sprue): two outer layers (bottom and top side) of about 1 mm thickness and a layer in the middle with a thickness of about 2 mm. In Figures 11(b) and 11(c), the surface and the middle layer for the sample “Delrin_IM_90°C-MT_S3” are shown with higher magnification. Differences in the spherulite size cannot be observed in these images. Because of their very small size, a quantitative estimation of the spherulite diameters was not possible in the light microscope. For the sake of completeness, it has to be mentioned that some white lines in Figure 8 like the ones in the middle of the samples “Delrin_IM_90°C-MT_S2” and “Delrin_IM_90°C-MT_S3” come from the sample preparation (microtome knife) and not from the processing. However, they can be identified rather easily because of their almost white color. No mentionable differences between the samples at the side positions (“S”) and those in the middle of the plate (“M”) were found.

The layer structure of the injection-molded Tenac plates, which is given in Figure 9, is quite different to that of Delrin. Similar to what was observed for polypropylene [26], a skin layer, a shear layer, and a spherulitic layer in the center of the plate can be observed for this material. The different layers are schematically illustrated in Figure 10. Interestingly, also the skin layer shows crystalline structures (refer to Figure 11(e) for higher magnification). For the shear layers, a slight decrease in thickness with increasing mold temperatures and between the “S1” and “S2” sample positions can be observed. However, far from the sprue (sample position “S3”), the shear layer is much thinner for all three mold temperatures. The strong decrease in the layer thickness from “S2” to “S3” is accompanied by a less compact spherulite structure in the shear layer. The spherulitic layer in the center of the plate has a similar morphology as the compression-molded

plate (Figures 7(c)–7(e)): comparably coarse spherulites, which are packed more and more compact from below the shear layer towards the center of the plate. The described microstructure is shown with higher magnification in Figures 11(d)–11(f). No influence of the mold temperature on the spherulitic layer can be observed except for the lowest one (60°C), where the spherulites in the center appear less compact. Far from the sprue (sample position “S3”), the spherulitic layer is significantly thicker than in the sample positions closer to the sprue (“S1” and “S2”). For Figures 11(e) and 11(f), the following spherulite diameters were estimated from the PLM images: shear layer around 40 μm , area in spherulitic layer directly below the shear layer around 50–70 μm , and spherulitic layer at some distance from shear layer around 70–130 μm . Also, for the Tenac samples, the influence of the sample preparation could not be avoided completely. Mainly for the 60°C mold temperature images, some scratches of the microtome knife are visible. For Tenac, the samples in the middle of the plate (“M”) showed some additional effects compared to those at the side positions (“S”). In both, the “M1” and the “M2” positions, the shear layers clearly become smaller with increasing mold temperature. Moreover, double shear layers at the bottom and at the top of the plate were found for the “M1” positions (near the sprue) for all three mold temperatures. Similar to the multiple shear layers observed for Delrin, this is related to the solidification of the outermost shear layer during the filling process of the mold.

3.1.3. DSC. The results of the DSC examination are summarized in Table 8 as average and standard deviation of the thirteen measurements conducted per sample position. As already mentioned in Section 2.2.3, the DSC examination was limited to selected processing conditions and sample positions. The reason for this was that in our previous research, DSC was found to be very insensitive to morphology changes in POM. However, as shown in Table 8, it was sufficiently sensitive to detect some differences in the crystallinity of the samples investigated. For both materials, the compression-molded samples had the highest degree of crystallinity. The difference between compression-molded samples and injection-molded ones was bigger in the case of Tenac. Comparing both materials, Delrin has slightly higher degrees of crystallinity in both the compression- and injection-molded samples. At least for the injection-molded plates analyzed, no crystallinity trend from near the sprue to far from the sprue is indicated by the results. For the interpretation of the results, it has to be kept in mind that some of the crystallinity differences documented in Table 8 are in the same order as the standard deviation.

3.2. Fatigue Fracture Tests. The results of the fatigue fracture tests of the Delrin and Tenac CT specimens are summarized in Figure 12. While there is rather little influence of the processing conditions on the lifetime of Delrin, the Tenac results show a clear dependence. For better illustration and because the logarithmic scale is usually misleading, the lifetime ratios between best and worst performing curves are exemplarily given in Table 9 for both materials. The required cycles to fracture values were calculated based on the fitting equations

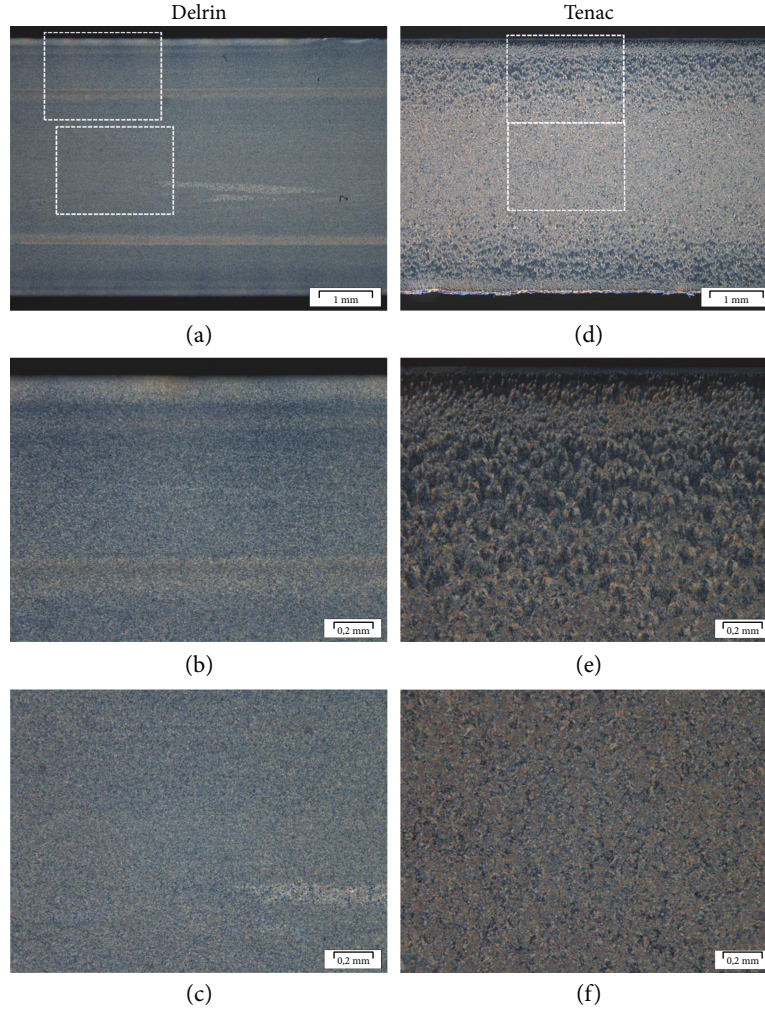


FIGURE 11: PLM images of the cross section of injection-molded plates. Overview and details for “Delrin_IM_90°C-MT_S3” (a–c) and “Tenac_IM_90°C-MT_S3” (d–f).

TABLE 8: DSC crystallinity of compression- and injection-molded POM plates.

Sample position	Crystallinity (%)	Standard deviation (%)
Delrin_CM_M	73.3	2.9
Delrin_IM_90°C-MT_S1	70.5	2.2
Delrin_IM_90°C-MT_S2	71.2	2.8
Delrin_IM_90°C-MT_S3	69.0	2.8
Tenac_CM_M	71.5	2.6
Tenac_IM_90°C-MT_S1	67.3	1.9
Tenac_IM_90°C-MT_S2	67.7	1.8
Tenac_IM_90°C-MT_S3	67.1	1.7

of the corresponding trend lines in Figure 12. The lifetime ratios were calculated for a specific ΔK_{init} value of $2.9 \text{ MPa m}^{0.5}$. This value was arbitrarily selected for comparison purposes. It is clear from Figure 12 that the lifetime ratios and even the best and worst performing curves are not uniform over the whole ΔK_{init} range examined. However,

Table 9 shows that for the ΔK_{init} value selected, the difference in the best and worst performing curves is about 10% for Delrin and almost 50% for Tenac. Obviously, the nucleation agent contained in Delrin reduces the processing sensitivity of the fatigue fracture properties significantly. On the other side, the variation of almost 50% in the lifetime of Tenac is quite a lot, when considering the rather moderate injection molding conditions used.

In the case of Delrin, the best performing processing condition was “Delrin_IM_110°C-MT.” It was slightly better than the other conditions, which did not differ significantly over a wide range of ΔK_{init} values. Nevertheless, “Delrin_IM_90°C-MT_Pos1-90°rot” showed a significantly reduced lifetime at the measurement point with the highest ΔK_{init} value. For the corresponding Tenac CT specimen of “Tenac_IM_90°C-MT_Pos1-90°rot,” this effect was even more distinct and it broke after a few thousand cycles (far below the scaling minimum of Figure 12(b)). For Tenac, the best performing curve was that of the compression-molded material (“Tenac_CM”). For small ΔK_{init} values, the worst performing curve was “Tenac_IM_60°C-MT.” This

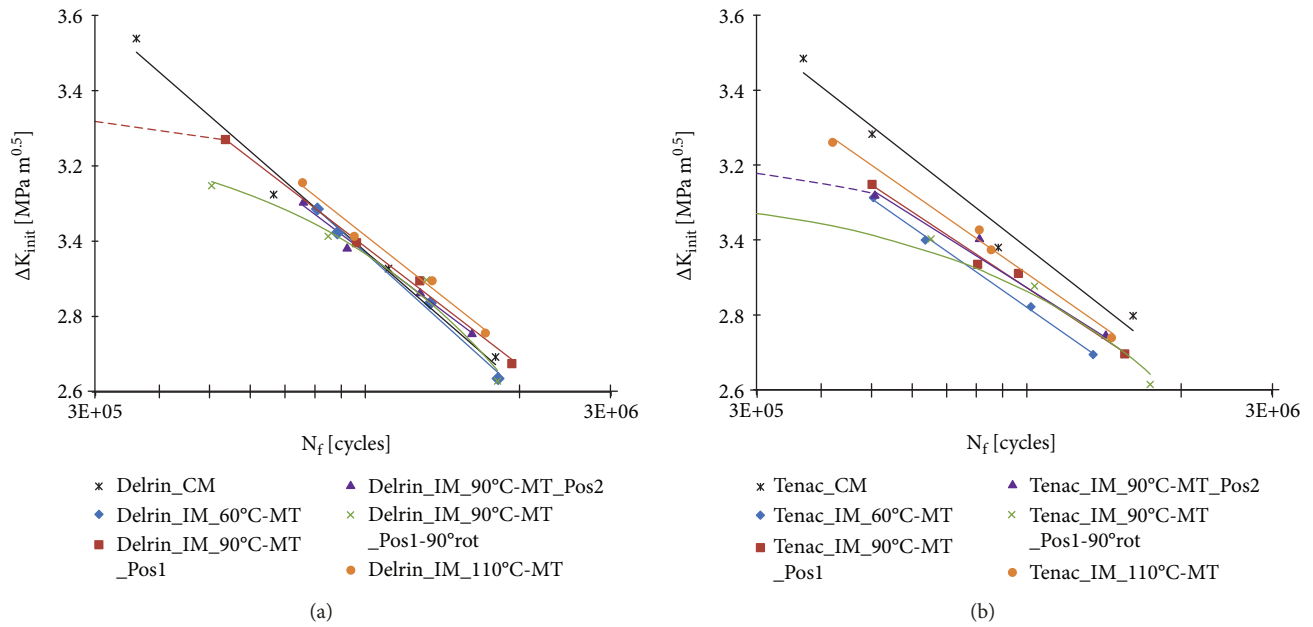


FIGURE 12: Fatigue fracture tests of CT specimens made of compression- and injection-molded plates. Results for Delrin (a) and Tenac (b).

TABLE 9: Lifetime ratios for Delrin and Tenac calculated for one specific ΔK_{init} value.

Resin	ΔK_{init} (MPa m ^{0.5})	Worst performing trend line	Best performing trend line	Lifetime ratio (Best/Worst * 100%)
Delrin	2.9	Delrin_IM_60°C-MT	Delrin_IM_110°C-MT	112%
Tenac	2.9	Tenac_IM_60°C-MT	Tenac_CM	145%

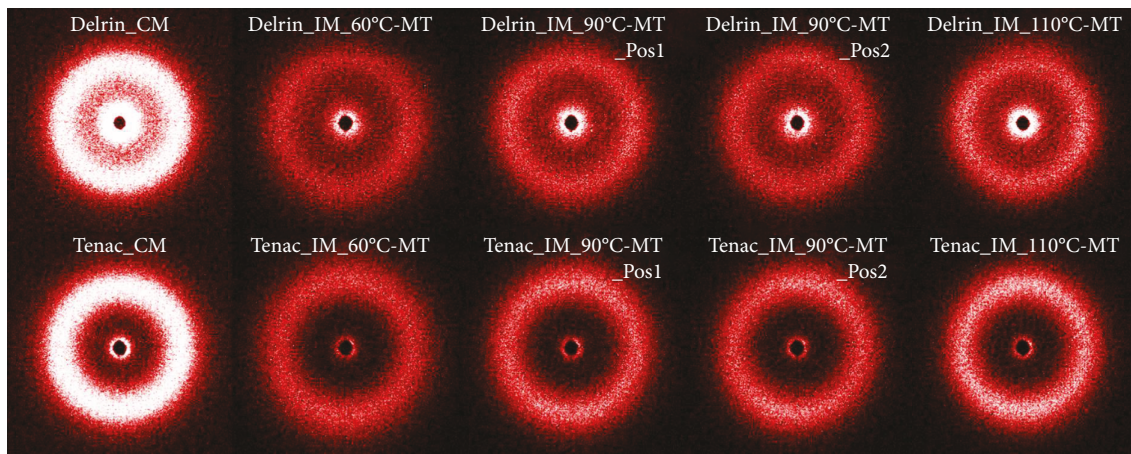


FIGURE 13: Representative SAXS patterns obtained for the different processing conditions.

changed abruptly with the kink in the “Tenac_IM_90°C-MT_Pos1-90°rot” curve at approximately 2.9–3.0 MPa m^{0.5}.

Interestingly, an abrupt decrease in the lifetime similar to that of the rotated specimens was also found for “Delrin_IM_90°C-MT_Pos1” and “Tenac_IM_90°C-MT_Pos2” during the conception phase of the fatigue fracture tests (the specimens broke after a few thousand cycles and thus far below the scaling minimums in Figure 12). This is indicated by the dashed lines in Figure 12, and it was the reason why the maximum ΔK_{init} values used for the tests of the

injection-molded specimens were lower than those of the compression-molded ones. Thus, the kink in the fatigue fracture curve is not a phenomenon of the rotated samples only. For the ΔK_{init} values examined, the compression-molded samples did not show any abrupt lifetime decrease. For the injection-molded specimens with 60°C and 110°C mold temperature, this additional information is not available. For the sake of completeness, it has to be mentioned that although the different injection molding conditions were all tested with identical load levels (refer to Table 5), some

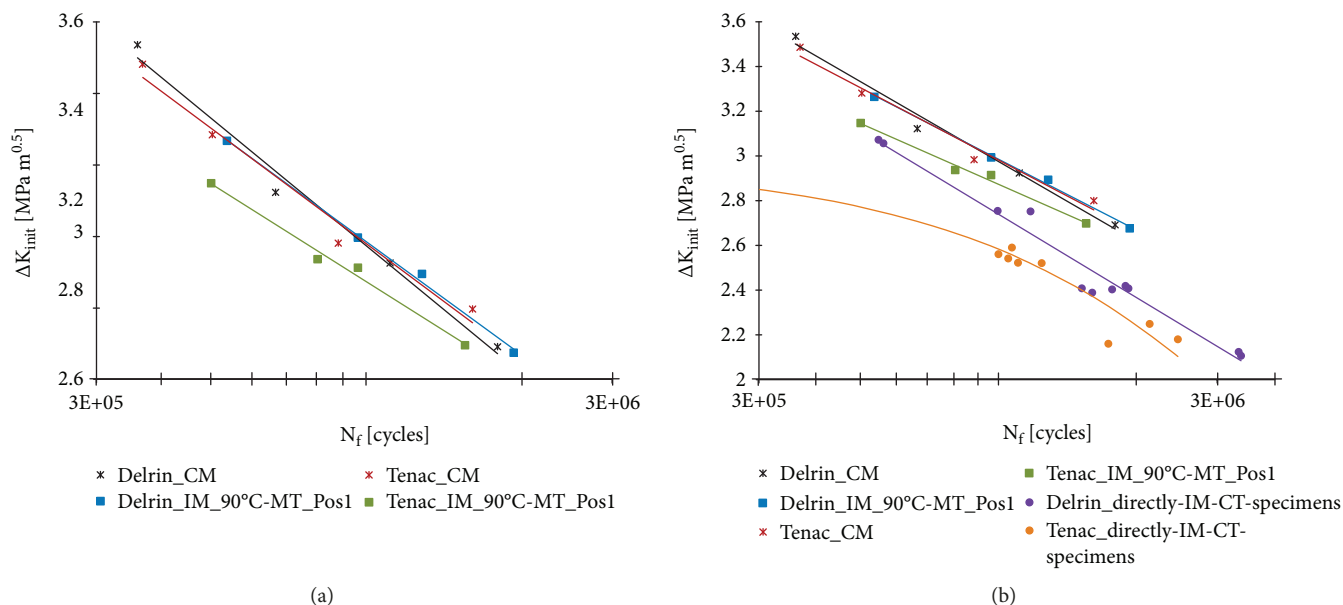


FIGURE 14: Comparison of fatigue fracture test results of Delrin and Tenac CT specimens. (a) Selected processing conditions used in this study. (b) Additional results obtained for directly injection-molded CT specimens produced under industrial conditions.

variation in the ΔK_{init} values can be observed in Figure 12. This variation was caused by different initial crack lengths introduced through the sharpening process of the notch using the razorblade.

Since no significant orientations could be detected using SAXS (Figure 13), the difference between the rotated and the not rotated (injection-molded) CT specimens was unexpected. However, despite the lack of (detectable) orientations, it is assumed that the difference was caused by the shear deformation in flow direction. It is speculated that during the filling process, the molecular orientation caused by this shear deformation was accompanied by partial molecular disentanglement through molecular slipping. While the orientations were obviously able to relax before the solidification (no trace in the SAXS images/profiles), these disentanglements were frozen in the crystallized polymer. Consequently, the molecules in flow direction were partially disentangled, which caused a decreased fatigue fracture performance for the rotated CT specimens with their crack plane orientation perpendicular to this direction.

The ability of the compression-molded samples to withstand even higher ΔK_{init} levels without showing a kink in the fatigue fracture curve is related to the higher quality of the crystal packing in comparison with the injection-molded samples. This higher crystal packing quality is deduced from the WAXD results; the compression-molded samples showed a higher contribution of higher diffraction peaks ((105), (115), and (205)). Additionally, in the SAXS 1D correlation results, the compression-molded samples had the biggest lamellar thicknesses, while the amorphous layer thicknesses were similar to the injection-molded samples.

For the injection-molded specimens, the lifetime differences at lower ΔK_{init} levels (Figure 12, below the kinks) are not reflected by the results of the morphology investigation.

For Delrin, the results of SAXS 1D correlation (Table 6) and WAXD (Table 7) show some reaction on the changed processing conditions but the fatigue fracture performance (Figure 12) almost does not. For Tenac, on the other hand, the SAXS 1D correlation results and the fatigue fracture curves change with the processing conditions but for the WAXD results there is only a slight change. Based on these results, it is concluded that, at least for the injection-molded specimens, the influence of the processing conditions on the fatigue fracture performance (at lower ΔK_{init} levels) cannot be explained by the morphology changes only. Since no orientations are indicated by the SAXS patterns in Figure 13, their influence is also excluded and the additional effects are attributed to residual stresses inside the specimens.

Indeed, the fatigue fracture performance of the injection-molded specimens in Figure 12 can be explained quite well by residual stresses, when taking into account the following considerations. The PLM images of the injection-molded plates (Figures 8 and 9) show a very homogeneous spherulite structure for Delrin, whereas it is rather inhomogeneous for Tenac. Hence, it is expected that the (nucleated) Delrin resin crystallizes and solidifies in a more uniform manner than the Tenac resin does. As a result, the residual stresses in the injection-molded Delrin plates are expected to be smaller and less dependent on the mold temperature than those in the injection-molded Tenac plates.

Based on these assumptions, in the following, the fatigue fracture curves are reinterpreted by taking into account the expected residual stress effects. The significant mold temperature dependence of the Tenac fatigue fracture curves observed in Figure 12 (while the corresponding WAXD crystallinity is almost unaffected) is related to a strong change in the residual stress level. According to the literature, the lower the mold temperature, the higher is the expected residual

stress level [53, 54] and for Tenac, the lower is the observed fatigue fracture performance. Hence, it is interpreted that there is an inverse proportionality between the fatigue fracture performance and the residual stress level, which is consistent with the effect of residual stresses on the tensile properties [55] and on the slow crack growth behavior of polymeric pipes [56, 57]. For Delrin, the insensitivity of the fatigue fracture curves to the mold temperature is, as described above, related to the nucleation of the material, which is expected to lead to a rather uniform residual stress level for the processing conditions examined. It has to be emphasized at this point that in terms of the morphology, the changes in dependence on the mold temperature were similar for Delrin and Tenac (SAXS 1D correlation, contribution of higher diffraction peaks to total crystallinity in WAXD) or even slightly higher for Delrin (WAXD total crystallinity).

To compare Delrin and Tenac directly, fatigue fracture curves of compression- and selected injection-molded CT specimens of both materials are plotted in Figure 14(a). Generally, the compression-molded samples are expected to reveal a very small (if at all) residual stress level, and the different morphologies in relation to the injection-molded samples were already discussed above. Interestingly, the compression-molded curves of both materials and the injection-molded one of Delrin practically coincide while the injection-molded one of Tenac has a worse fatigue fracture performance. The coincidence of the compression-molded curves is not surprising when considering the similar WAXD results, the mentioned small residual stress level expected, and the similar molecular weight and polydispersity of both resins (Section 2.1). Obviously, the differences in terms of the SAXS 1D correlation results do not significantly affect the fatigue fracture performance. Taking into account the completely different spherulite sizes and distributions shown by the PLM images in Figure 7, it is confirmed what has already been observed by other authors [13, 19]; at least for POM, there is no direct influence of the spherulite size and distribution on the fracture mechanical properties. This is plausible because in POM and other polymeric materials, the crack path was found to run through the spherulites [8, 11, 12, 18, 58–61] as long as the latter do not pass a distinct level of size and crystalline perfection [18, 58]. The additional coincidence of the injection-molded Delrin curve with the compression-molded ones is not surprising from the point of the total WAXD crystallinity. However, there are also morphological differences: the already mentioned lower contribution of the higher WAXD peaks to the total crystallinity (interpreted as lower quality in the crystal packing) and clear differences in the SAXS 1D correlation results. The level of the residual stresses in the injection-molded Delrin specimens is unknown especially since the nucleated Delrin resin seems to be less prone to the generation of residual stresses than the Tenac resin (details were discussed above). Hence, it is speculated that either the morphological differences between the compression- and the selected injection-molded Delrin specimens do not significantly affect the fatigue fracture curves and/or that they are compensated by residual stress effects. The worse fatigue fracture performance

of the injection-molded Tenac specimens in comparison to the compression-molded curves is interpreted as a combined effect of different morphologies (smaller total crystallinity and lower contribution of the higher diffraction peaks to the total crystallinity in WAXD, clear differences in the SAXS 1D correlation results) and different residual stress levels.

In Figure 14(b), fatigue fracture curves of directly injection-molded CT specimens of Delrin and Tenac are added to the curves of Figure 14(a). The Tenac curve was already published previously together with information concerning processing conditions, specimen mold design (crack growth perpendicular to flow direction), and morphological details [15]. For the directly injection-molded Delrin specimens, the same processing conditions and mold design were used. The important point is that technical conditions with much smaller cycle times than in our study were used for the processing. It is obvious that this has a much stronger influence on the fatigue fracture performance than the comparatively small processing variations used in our study. The comparison with the directly injection-molded specimens is intended as outlook to demonstrate the wide field in which the fatigue fracture performance of unfilled POM can be varied (logarithmic scale on x -axis) only by modifying the processing conditions.

4. Conclusions

Quadratic plates of two POM homopolymer resins (Delrin and Tenac) were produced by compression molding and by injection molding under moderate conditions. The injection molding was conducted with three different mold temperatures. At specific locations, the plates were analyzed concerning their morphological structures on the micro- (spherulite size and distribution, processing layer structure/PLM) and nanolevel (long period, lamellar thickness, and amorphous layer thickness/SAXS), concerning their crystallinity (DSC, SAXS, and WAXD) and concerning their fatigue fracture properties. For the latter, CT specimens were cut out from the plates at defined positions. The PLM images showed distinct differences between the resins and between compression and injection molding, while for SAXS and WAXD, the differences were much smaller. Concerning the fatigue fracture performance, the Delrin resin showed only a small dependence on the processing conditions. For Tenac, on the other hand, this dependence was more pronounced. The differences in this dependence could not be explained by morphological considerations alone. Since no evidence for orientations was found in the SAXS patterns, it was concluded that residual stresses had to be responsible for them. Because the nucleated Delrin resin revealed less dependence of the fatigue fracture performance on the processing conditions than the Tenac resin (in combination with similar morphological changes), it was further concluded that the nucleation caused a reduced residual stress level in the plates. This was explained by a more uniform solidification in the mold because of the faster crystallization in the presence of the nucleation agent.

As a general conclusion, for future studies in which the influence of the processing conditions on the (fracture)

mechanical behavior of polymers is examined, it is strongly suggested to combine the morphological analysis with residual stress measurements, especially when injection molding is involved. For the interpretation of the SAXS and WAXD results, it has to be kept in mind that the whole cross section was examined. Hence, the quantitative results for crystallinities, long periods, layer thicknesses, and diffraction peak contributions (to the overall crystallinity) represent average values along the thickness. A local layer-by-layer analysis could help in the interpretation of the morphology data. However, a follow-up study showed that such layer-by-layer analyses are error-prone, and significant method improvement is needed to obtain reliable results. The 3-component model fitting, which was used in this study as an alternative method to analyze the SAXS profiles of POM (and which was developed especially for POM [21, 45, 46]), did not provide acceptable fitting results. The authors doubt its applicability to high molecular weight resins of POM.

Data Availability

The underlying data of this study was measured and determined during an industrial research project. Hence, it is not publically available.

Disclosure

A part of this paper was previously presented as a Poster at the 17th International Conference on Deformation, Yield and Fracture of Polymers (25th to 29th of March 2018 in Kerkrade/Netherlands).

Conflicts of Interest

The authors declare that there is no conflict of interest regarding the publication of this paper.

Acknowledgments

The research work was performed at the Polymer Competence Center Leoben GmbH (PCCL, Austria) within the framework of the COMET-program of the Federal Ministry for Transport, Innovation and Technology and Federal Ministry for Economy, Family and Youth with contributions by the Montanuniversitaet Leoben (Institute of Materials Science and Testing of Polymers). The PCCL is funded by the Austrian Government and the State Governments of Styria, Lower Austria and Upper Austria.

Supplementary Materials

A graphical abstract of the present study is added as supplementary material. (*Supplementary Materials*)

References

- [1] S. Lüftl, P. M. Visakh, and S. Chandran, *Polyoxymethylene Handbook: Structure, Properties, Applications and Its Nanocomposites*, John Wiley & Sons, Hoboken, NJ, USA, 2013.
- [2] J. Rösler, *Zur Tragfähigkeitssteigerung Thermoplastischer Zahnräder mit Füllstoffen*, Technische Universität Berlin, 2005, Dissertation.
- [3] B. Heym and W. Beitz, "Zur belastbarkeit von stirnzahnrädern aus dem hochtemperatur-thermoplast PEEK," *Konstruktion*, vol. 47, pp. 351–357, 1995.
- [4] M. Berer and Z. Major, "Characterization of the global deformation behaviour of engineering plastics rolls," *International Journal of Mechanics and Materials in Design*, vol. 6, no. 1, pp. 1–9, 2010.
- [5] M. Berer and Z. Major, "Characterisation of the local deformation behaviour of engineering plastics rolls," *Strain*, vol. 48, no. 3, pp. 225–234, 2012.
- [6] M. Berer, I. Mitev, and G. Pinter, "Finite element study of mode I crack opening effects in compression-loaded cracked cylinders," *Engineering Fracture Mechanics*, vol. 175, pp. 1–14, 2017.
- [7] B. Ramoa, M. Berer, M. Schwaiger, and G. Pinter, "Effect of cyclic fatigue on the fracture toughness of Polyoxymethylene," *Journal of Physics: Conference Series*, vol. 843, article 012052, 2017.
- [8] P. E. Bretz, R. W. Hertzberg, and J. A. Manson, "The effect of molecular weight on fatigue crack propagation in nylon 66 and polyacetal," *Journal of Applied Polymer Science*, vol. 27, no. 5, pp. 1707–1717, 1982.
- [9] S. Bandyopadhyay, J. R. Roseblade, and R. Muscat, "Fracture study of a polyacetal resin," *Journal of Materials Science*, vol. 28, no. 14, pp. 3777–3782, 1993.
- [10] S. Hashemi and J. G. Williams, "Size and loading mode effects in fracture toughness testing of polymers," *Journal of Materials Science*, vol. 19, no. 11, pp. 3746–3759, 1984.
- [11] R. W. Hertzberg, M. D. Skibo, and J. A. Manson, "Fatigue crack propagation in polyacetal," *Journal of Materials Science*, vol. 13, no. 5, pp. 1038–1044, 1978.
- [12] A. Lazzeri, A. Marchetti, and G. Levita, "Fatigue and fracture in polyacetal resins," *Fatigue and Fracture of Engineering Materials and Structures*, vol. 20, no. 8, pp. 1207–1216, 1997.
- [13] J. Runt and K. P. Gallagher, "The influence of microstructure on fatigue crack propagation in polyoxymethylene," *Journal of Materials Science*, vol. 26, no. 3, pp. 792–798, 1991.
- [14] M. Berer and G. Pinter, "Determination of crack growth kinetics in non-reinforced semi-crystalline thermoplastics using the linear elastic fracture mechanics (LEFM) approach," *Polymer Testing*, vol. 32, no. 5, pp. 870–879, 2013.
- [15] M. Berer, G. Pinter, and M. Feuchter, "Fracture mechanical analysis of two commercial polyoxymethylene homopolymer resins," *Journal of Applied Polymer Science*, vol. 131, no. 19, pp. 1–15, 2014.
- [16] F. Arbeiter, B. Schritteser, A. Frank, M. Berer, and G. Pinter, "Cyclic tests on cracked round bars as a quick tool to assess the long term behaviour of thermoplastics and elastomers," *Polymer Testing*, vol. 45, pp. 83–92, 2015.
- [17] J. Runt and M. Jacq, "Effect of crystalline morphology on fatigue crack propagation in polyethylene," *Journal of Materials Science*, vol. 24, no. 4, pp. 1421–1428, 1989.
- [18] R. Greco and G. Ragosta, "Isotactic polypropylenes of different molecular characteristics: influence of crystallization conditions and annealing on the fracture behaviour," *Journal of Materials Science*, vol. 23, no. 11, pp. 4171–4180, 1988.
- [19] C. J. G. Plummer, P. Menu, N. Cudré-Mauroux, and H. H. Kausch, "The effect of crystallization conditions on the

- properties of polyoxymethylene,” *Journal of Applied Polymer Science*, vol. 55, no. 3, pp. 489–500, 1995.
- [20] R. Seguela, “Critical review of the molecular topology of semicrystalline polymers: the origin and assessment of intercrystalline tie molecules and chain entanglements,” *Journal of Polymer Science Part B: Polymer Physics*, vol. 43, no. 14, pp. 1729–1748, 2005.
- [21] H. Hama and K. Tashiro, “Structural changes in non-isothermal crystallization process of melt-cooled polyoxymethylene [II] evolution of lamellar stacking structure derived from SAXS and WAXS data analysis,” *Polymer*, vol. 44, no. 7, pp. 2159–2168, 2003.
- [22] G. Kalay and M. J. Bevis, “Injection molding of isotactic polypropylene,” in *Polypropylene*, Polymer Science and Technology Series, J. Karger-Kocsis, Ed., pp. 329–334, Springer, Dordrecht, 1999.
- [23] D. G. M. Wright, R. Dunk, D. Bouvart, and M. Autran, “The effect of crystallinity on the properties of injection moulded polypropylene and polyacetal,” *Polymer*, vol. 29, no. 5, pp. 793–796, 1988.
- [24] R. Čermák, M. Obadal, P. Ponižil, M. Polášková, K. Stoklasa, and A. Lengálová, “Injection-moulded α - and β -polypropylenes: I. structure vs. processing parameters,” *European Polymer Journal*, vol. 41, no. 8, pp. 1838–1845, 2005.
- [25] G. Kalay and M. J. Bevis, “Processing and physical property relationships in injection-molded isotactic polypropylene. 2. Morphology and crystallinity,” *Journal of Polymer Science Part B: Polymer Physics*, vol. 35, no. 2, pp. 265–291, 1997.
- [26] S. Liparoti, A. Sorrentino, G. Guzman, M. Cakmak, and G. Titomanlio, “Fast mold surface temperature evolution: relevance of asymmetric surface heating for morphology of iPP molded samples,” *RSC Advances*, vol. 5, no. 46, pp. 36434–36448, 2015.
- [27] R. Pantani, I. Coccorullo, V. Speranza, and G. Titomanlio, “Modeling of morphology evolution in the injection molding process of thermoplastic polymers,” *Progress in Polymer Science*, vol. 30, no. 12, pp. 1185–1222, 2005.
- [28] R. Čermák, M. Obadal, P. Ponižil, M. Polášková, K. Stoklasa, and J. Hečková, “Injection-moulded α - and β -polypropylenes: II. Tensile properties vs. processing parameters,” *European Polymer Journal*, vol. 42, no. 9, pp. 2185–2191, 2006.
- [29] G. Kalay and M. J. Bevis, “Processing and physical property relationships in injection-molded isotactic polypropylene. 1. Mechanical properties,” *Journal of Polymer Science Part B: Polymer Physics*, vol. 35, no. 2, pp. 241–263, 1997.
- [30] J.-W. Housmans, M. Gahleitner, G. W. M. Peters, and H. E. H. Meijer, “Structure–property relations in molded, nucleated isotactic polypropylene,” *Polymer*, vol. 50, no. 10, pp. 2304–2319, 2009.
- [31] M. Fujiyama, T. Wakino, and Y. Kawasaki, “Structure of skin layer in injection-molded polypropylene,” *Journal of Applied Polymer Science*, vol. 35, no. 1, pp. 29–49, 1988.
- [32] J. C. Viana, A. M. Cunha, and N. Billon, “The tensile behaviour of an injection-moulded propylene-ethylene copolymer: the effect of the local thermomechanical processing conditions,” *Polymer International*, vol. 43, no. 2, pp. 159–166, 1997.
- [33] J. C. Viana, A. M. Cunha, and N. Billon, “The effect of the skin thickness and spherulite size on the mechanical properties of injection mouldings,” *Journal of Materials Science*, vol. 36, no. 18, pp. 4411–4418, 2001.
- [34] J. C. Viana, A. M. Cunha, and N. Billon, “The thermomechanical environment and the microstructure of an injection moulded polypropylene copolymer,” *Polymer*, vol. 43, no. 15, pp. 4185–4196, 2002.
- [35] J. C. Viana, N. Billon, and A. M. Cunha, “The thermomechanical environment and the mechanical properties of injection moldings,” *Polymer Engineering & Science*, vol. 44, no. 8, pp. 1522–1533, 2004.
- [36] W.-W. Tseng, *Relationships between Processing, Structure, Fatigue Crack Growth and J-Integral Fracture Toughness of Neat Polyetheretherketone*, University of Texas, 1986, Dissertation.
- [37] B. Ozcelik, A. Ozbay, and E. Demirbas, “Influence of injection parameters and mold materials on mechanical properties of ABS in plastic injection molding,” *International Communications in Heat and Mass Transfer*, vol. 37, no. 9, pp. 1359–1365, 2010.
- [38] C. J. G. Plummer, P. Béguelin, and H.-H. Kausch, “The temperature and strain-rate dependence of mechanical properties in polyoxymethylene,” *Polymer Engineering and Science*, vol. 35, no. 16, pp. 1300–1312, 1995.
- [39] J. C. Viana, “The local thermomechanical conditions and the fracture behavior of an injection-molded poly(oxymethylene),” *Polymer Engineering and Science*, vol. 46, no. 2, pp. 181–187, 2006.
- [40] X. Zhao and L. Ye, “Structure and properties of highly oriented polyoxymethylene produced by hot stretching,” *Materials Science and Engineering: A*, vol. 528, no. 13–14, pp. 4585–4591, 2011.
- [41] M. Halb, *Influence of the Processing Conditions on Morphology and Fracture Mechanical Properties of Unfilled Polyoxymethylene (POM)*, [Ph.D. Thesis], Montanuniversitaet Leoben, 2016.
- [42] A. P. Hammersley, “FIT2D: a multi-purpose data reduction, analysis and visualization program,” *Journal of Applied Crystallography*, vol. 49, no. 2, pp. 646–652, 2016.
- [43] C. G. Vonk and G. Kortleve, “X-ray small-angle scattering of bulk polyethylene,” *Kolloid-Zeitschrift & Zeitschrift für Polymere*, vol. 220, no. 1, pp. 19–24, 1967.
- [44] G. R. Strobl and M. Schneider, “Direct evaluation of the electron density correlation function of partially crystalline polymers,” *Journal of Polymer Science: Polymer Physics Edition*, vol. 18, no. 6, pp. 1343–1359, 1980.
- [45] H. Hama and K. Tashiro, “Structural changes in non-isothermal crystallization process of melt-cooled polyoxymethylene. [I] Detection of infrared bands characteristic of folded and extended chain crystal morphologies and extraction of a lamellar stacking model,” *Polymer*, vol. 44, no. 10, pp. 3107–3116, 2003.
- [46] H. Hama and K. Tashiro, “Structural changes in isothermal crystallization process of polyoxymethylene investigated by time-resolved FTIR, SAXS and WAXS measurements,” *Polymer*, vol. 44, no. 22, pp. 6973–6988, 2003.
- [47] M. Shimomura, *Morphology Dependence of Vibrational Spectra of Polyoxymethylene and P(Ethylene Oxide) Crystals*, Osaka University, 1993, Dissertation.
- [48] J. T. Koberstein, B. Morra, and R. S. Stein, “The determination of diffuse-boundary thicknesses of polymers by small-angle X-ray scattering,” *Journal of Applied Crystallography*, vol. 13, no. 1, pp. 34–45, 1980.
- [49] B. Goderis, H. Reynaers, M. H. J. Koch, and V. B. F. Mathot, “Use of SAXS and linear correlation functions for the

- determination of the crystallinity and morphology of semi-crystalline polymers. Application to linear polyethylene,” *Journal of Polymer Science Part B: Polymer Physics*, vol. 37, no. 14, pp. 1715–1738, 1999.
- [50] N. Stribeck, *X-Ray Scattering of Soft Matter*, Springer, Berlin, Heidelberg, 2007.
- [51] J. Karger-Kocsis, R. Walter, and K. Friedrich, “Annealing effects on the fatigue crack propagation of injection moulded PEEK and its short-fibre composites,” *Journal of Polymer Engineering*, vol. 8, no. 3-4, pp. 221–255, 1988.
- [52] International Standard, *Polyethylene (PE) Materials — Determination of Resistance to Slow Crack Growth under Cyclic Loading — Cracked Round Bar Test Method*, International Organization for Standardization, 2015, no. 18489.
- [53] A. Siegmann, A. Buchman, and S. Kenig, “Residual stresses in polymers I: the effect of thermal history,” *Polymer Engineering and Science*, vol. 22, no. 1, pp. 40–47, 1982.
- [54] A. Siegmann, A. Buchman, and S. Kenig, “Residual stresses in polymers III: the influence of injection-molding process conditions,” *Polymer Engineering and Science*, vol. 22, no. 9, pp. 560–568, 1982.
- [55] A. Siegmann, A. Buchman, and S. Kenig, “Residual stresses in polymers. II. Their effect on mechanical behavior,” *Polymer Engineering and Science*, vol. 21, no. 15, pp. 997–1002, 1981.
- [56] P. Hutař, M. Ševčík, A. Frank, L. Náhlík, J. Kučera, and G. Pinter, “The effect of residual stress on polymer pipe lifetime,” *Engineering Fracture Mechanics*, vol. 108, pp. 98–108, 2013.
- [57] J. Poduška, P. Hutař, J. Kučera et al., “Residual stress in polyethylene pipes,” *Polymer Testing*, vol. 54, pp. 288–295, 2016.
- [58] C. J. G. Plummer, N. Cudré-Mauroux, and H.-H. Kausch, “Deformation and entanglement in semicrystalline polymers,” *Polymer Engineering and Science*, vol. 34, no. 4, pp. 318–329, 1994.
- [59] S. Bandyopadhyay and H. R. Brown, “Studies of environmental stress-crack propagation in low-density polyethylene,” *Journal of Polymer Science: Polymer Physics Edition*, vol. 19, no. 5, pp. 749–761, 1981.
- [60] P. J. Rae, E. N. Brown, and E. B. Orler, “The mechanical properties of poly(ether-ether-ketone) (PEEK) with emphasis on the large compressive strain response,” *Polymer*, vol. 48, no. 2, pp. 598–615, 2007.
- [61] N. A. Jones and A. J. Lesser, “Morphological study of fatigue-induced damage in isotactic polypropylene,” *Journal of Polymer Science Part B: Polymer Physics*, vol. 36, no. 15, pp. 2751–2760, 1998.

